

# The Stellar Content of Obscured Galactic Giant H II Regions IV.: NGC3576

E. Figuerêdo

*IAG-USP, R. do Matão 1226, 05508-900, São Paulo, Brazil*

R. D. Blum<sup>1</sup>

*Cerro Tololo Interamerican Observatory, Casilla 603, La Serena, Chile*

A. Damineli<sup>1</sup>

*IAG-USP, R. do Matão 1226, 05508-900, São Paulo, Brazil*

and

P. S. Conti

*JILA, University of Colorado  
Campus Box 440, Boulder, CO, 80309*

## ABSTRACT

We present deep, high angular resolution near-infrared images of the obscured Galactic Giant H II region NGC3576. Our images reach objects to  $\sim 3M_{\odot}$ . We collected high signal-to-noise  $K$ -band spectra of eight of the brightest objects, some of which are affected by excess emission and some which follow a normal interstellar reddening law. None of them displayed photospheric features typical of massive OB type stars. This indicates that they are still enshrouded in their natal cocoons. The  $K$ -band brightest source (NGC3576#48) shows CO 2.3  $\mu\text{m}$  bandhead emission, and three others have the same CO feature in absorption. Three sources display spatially unresolved  $H_2$  emission, suggesting dense shocked regions close to the stars. We conclude that the remarkable object NGC3576#48 is an early-B/late-O star surrounded by a thick circumstellar disk. A number of other relatively bright cluster members also display excess emission in the  $K$ -band, indicative of reprocessing disks around massive stars (YSOs). Such emission appears common in other Galactic Giant H II regions we have surveyed. The IMF slope of the cluster,  $\Gamma = -1.51$ , is consistent with Salpeter's distribution and similar to what has been observed in the Magellanic Cloud clusters and in the periphery of our Galaxy.

*Subject headings:* H II regions — infrared: stars — stars: early-type — stars: fundamental parameters — stars: formation

---

<sup>1</sup>Visiting Astronomer, Cerro Tololo Inter-American Observatory, National Optical Astronomy Observatories, which is operated by Associated Universities for Research in Astronomy, Inc., under cooperative agreement with the National Science Foundation.

## 1. Introduction

Massive stars have a strong impact on the evolution of galaxies. O-type stars and their descendants, the Wolf-Rayet stars, are the main source of UV photons, mass, energy and momentum to the interstellar medium. They play the main role in the ionization of the interstellar medium and dust heating. The Milky Way is the best place to access, simultaneously, massive stellar populations and their impact on the surrounding gas and dust. The sun’s position in the Galactic plane, however, produces a heavy obscuration in the optical window ( $A_V \approx 20 - 40$  mag) toward the inner Galaxy, where massive star formation activity is the greatest. Shifting to longer wavelengths, the perspective is much better, especially in the near infrared, because these wavelengths are long enough to lessen the effect of interstellar extinction ( $A_K \approx 2 - 4$  mag) and still short enough to probe the stellar photospheric features of massive stars (Hanson et al. 1996).

The study of Giant H II regions (GH II) in the near-infrared can address important astrophysical questions such as: 1. characterizing the stellar content by deriving the initial mass function (IMF), star formation rate and age; 2. determining the physical processes involved in the formation of massive stars, through the identification of OB stars in very early evolutionary stages, such as embedded young stellar objects (YSOs) and ultra-compact H II regions (UCH II); and 3. tracing the spiral arms of the Galaxy by measuring spectroscopic parallaxes of zero age main sequence OB stars. The exploration of the stellar content of obscured Galactic GH II regions has been studied recently by several groups: Hanson et al. (1997), (Blum et al. 1999, 2000, 2001), Okumura et al. (2000). In particular, Blum and collaborators presented near infrared imaging and spectroscopic observations of three optically obscured GH II regions: W43, W42 and W31. These observations revealed massive star clusters at the center of the H II regions which had been previously discovered and studied only at longer wavelengths.

In this work, we present results for NGC3576 (G291.3-0.71), located at a kinematic distance  $2.8 \pm 0.3$  kpc, which we adopted from De Pree et al. (1999), after correcting for the standard Galactic center distance ( $R_0 = 8$  kpc). NGC3576 appears in the visible passbands as a faint H II region, but in the infrared it is among the most luminous in our Galaxy (Goss & Radhakrishnan 1969). In fact, with  $1.6 \times 10^{50}$  photons  $s^{-1}$  inferred from the radio data, it can be classified as a GH II (following the suggestion of R. Kennicutt for sources brighter than  $10^{50}$  Lyman continuum, =  $L_{yc}$ , photons per second). A GH II region has at least ten times the luminosity of the Orion nebula and roughly the number emitted from the hottest single O3-type star, thus implying multiple hot stars.

NGC3576 was observed in the radio continuum by Goss & Shaver (1970). McGee & Gardner (1968), McGee & Newton (1981), Wilson et al. (1970), and De Pree et al. (1999) have detected radio recombination lines. Maser sources have also been detected in the region: CH<sub>3</sub>OH (Caswell et al. 1995) and H<sub>2</sub>O (Caswell et al. 1989). The detection of intense emission in the 10  $\mu$ m window, H<sub>2</sub>O masers, and the compact thermal emission in the radio are typical indications of the primitive stages of star formation and of a dense circumstellar environment. Photometry from 1 to 2.5  $\mu$ m of the brightest sources was performed by Moorwood & Salinari (1981) and by Persi et al. (1994) showing

that the spectral energy distributions of these objects suggests that they have excess emission. An intense CO J=2–1 line at 230 GHz was observed by White & Phillips (1983) in the core region of NGC3576.

In the present paper, we present an investigation of the stellar content of NGC3576 through the *J*, *H* and *K* imaging and *K*–band spectroscopy (described in §2). In §3 we discuss our results, and our conclusions are summarized in §4.

## 2. Observations and Data Reduction

*J* ( $\lambda \approx 1.3 \mu\text{m}$ ,  $\Delta\lambda \approx 0.3 \mu\text{m}$ ), *H* ( $\lambda \approx 1.6 \mu\text{m}$ ,  $\Delta\lambda \approx 0.3 \mu\text{m}$ ) and *K* ( $\lambda \approx 2.1 \mu\text{m}$ ,  $\Delta\lambda \approx 0.4 \mu\text{m}$ ) images of NGC3576 were obtained on the nights of 1999 March 3 and 4 and 2000 May 19 and 20 with the f/14 tip–tilt system on the Cerro Tololo Interamerican Observatory (CTIO) 4-m Blanco Telescope using the facility imager OSIRIS<sup>2</sup>) and on the nights of 1998 July 9 to 13 with the facility imager CIRIM<sup>3</sup>) mounted on the 1.5-m telescope. Spectroscopic data were obtained with the Blanco telescope and the facility near infrared spectrometer, IRS, in 1998 May 17 and June 2–3, and with OSIRIS using the f/14 tip–tilt system in 1999 March 3–4, 1999 May 2–3, and 2001 July 7 and 12. OSIRIS delivers a plate scale of  $0.16''/\text{pixel}$ , the IRS  $0.32''/\text{pixel}$ , and CIRIM  $1.16''/\text{pixel}$ .

All basic data reduction was accomplished using IRAF<sup>4</sup>. Each image was flat-fielded using dome flats and then sky subtracted using a median-combined image of five to six frames. Independent sky frames were obtained 5–10' south of the NGC3576 cluster.

### 2.1. Imaging

The OSIRIS 1999 March images were obtained under photometric conditions. Total exposure times were 180s, 45s and 45s at *J*, *H* and *K*, respectively. The individual *J*, *H* and *K* frames were shifted and combined. These combined frames have point sources with FWHM of  $\approx 0.61''$ ,  $0.88''$  and  $0.64''$  at *J*, *H* and *K*, respectively. DoPHOT (Schechter et al. 1993) photometry was performed on the combined images. The flux calibration was accomplished using standard star GSPC S427-D (also known as [PMK98] 9123) from Persson et al. (1998) which is on the Las Campanas Observatory photometric system (LCO). The LCO standards are essentially on the

---

<sup>2</sup>OSIRIS is a collaborative project between Ohio State University and CTIO. Osiris was developed through NSF grants AST 90-16112 and AST 92-18449.

<sup>3</sup>CIRIM and OSIRIS are described in the instrument manuals found on the CTIO WWW site at [www.ctio.noao.edu](http://www.ctio.noao.edu). For OSIRIS, see also (DePoy et al. 1993).

<sup>4</sup>IRAF is distributed by the National Optical Astronomy Observatories.

CIT/CTIO photometric system (Elias et al. 1982), though color transformations exist between the two systems for redder stars. No transformation exists between OSIRIS and either CIT/CTIO or LCO systems.

The standard observations were made just after the NGC3576 data and within 0.24 airmass from the target. No corrections were applied for these small difference in airmass. Aperture corrections measured inside 20 pixel radius circles were used to put the instrumental magnitudes on a flux scale. Six uncrowded stars on the NGC3576 images were used for this purpose. Since the brightest stars in the 1999 images were saturated, we have taken short exposure images in May 2000. Although the conditions in May 2000 were non-photometric, we used stars in common with the 1999 images to determine the zero point for the additional (bright) stars.

Uncertainties for the  $J$ ,  $H$  and  $K$  magnitudes in 1999 images include the formal DoPHOT error added in quadrature to the error in the mean of the photometric standard and to the uncertainty of the aperture correction used in transforming from the DoPHOT photometry to OSIRIS magnitudes. The sum in quadrature of the aperture correction and standard star uncertainties are  $\pm 0.032$ ,  $\pm 0.034$  and  $\pm 0.069$  mag in  $J$ ,  $H$  and  $K$ , respectively. The scatter in the instrumental magnitudes in the set of stars from the 1999 images used to calibrate the May 2000 images are  $\pm 0.010$  ( $J$ ),  $\pm 0.012$  ( $H$ ) and  $\pm 0.010$  ( $K$ ) mag; thus the errors in the bright star magnitudes are dominated by the uncertainty in the standard stars. The DoPHOT errors ranged from approximately  $\pm 0.01$  mag to an arbitrary cutoff of 0.2 mag (stars with larger errors were excluded from further analysis).

Lower angular resolution images were obtained at  $J$ ,  $H$  and  $K$  using CIRIM at f/8 on the CTIO 1.5-m telescope ( $1.16''$  pixel $^{-1}$ ). The individual frames in each filter were shifted and combined and have measured seeing of  $2.2''$  FWHM. Although collected under photometric conditions, these images are not as deep as that of the 4-m telescope and were used only to transform to equatorial coordinates, since they encompassed a wider field than the OSIRIS images taken at the 4-m telescope.

## 2.2. Spectroscopy

The  $K$ -band spectra of eight of the brightest stars in the NGC3576 cluster were obtained: #11, #48, #69 and #160 with the IRS and #4, #48, #78, #95 and #184 with OSIRIS. The spectra were divided by the average continuum of several A-type stars to remove telluric absorption. The Br $\gamma$  photospheric feature was removed from the average A-type star spectrum by eye by drawing a line between two continuum points. One dimensional spectra were obtained by extracting and summing the flux in  $\pm 2$  pixel aperture. The extractions include background subtraction from apertures, 1-2'' on either side of the object.

The wavelength calibration was accomplished by measuring the position of bright OH $^-$  lines from the  $K$ -band sky spectrum (Olivia & Origlia 1992). The spectral resolution at  $2.2 \mu\text{m}$  is  $\lambda/\Delta\lambda \approx 3000$  for OSIRIS and  $\lambda/\Delta\lambda \approx 825$  for the IRS.

### 3. Results

#### 3.1. Near-infrared Imaging

The OSIRIS  $J$ ,  $H$  and  $K$ –band images reveal an embedded star cluster. We detected 315 stars in the  $K$ –band to a limiting magnitude of 16 (see below) in a region of 0.03 square degrees. Figure 1 shows a finding chart using the  $K$ –band image. A false color image is presented in Figure 2, made by combining the three near infrared images and adopting the colors blue, green and red, for  $J$ ,  $H$ , and  $K$ , respectively. In this way, the bluest stars are likely foreground objects, and the reddest stars are probably  $K$ –band excess objects, indicating the presence of hot dust for objects recently formed in the cluster (background objects seen through a high column of interstellar dust would also appear red). The diffuse nebula is mainly due to  $\text{Br}\gamma$  emission in the H II region. The dark patches in the bottom right of Figure 2 are zones of the giant molecular cloud from which NGC3576 is emerging. There is no doubt that this is a signature of a young cluster containing massive stars, now in the process of shredding the local molecular cloud. The cluster is asymmetric, with the majority of the stars encompassed in a semi circle; and there is a definite appearance that the cluster is destroying the cloud from the NE to the SW. The NE is also the direction toward which the H II region is seen in the visual.

The  $H - K$  versus  $K$  color magnitude diagram (CMD) is displayed in Figure 3. The open circles indicate objects fainter than  $H = 15$ . A concentration of dots appear around  $H - K = 1$ , probably indicating the average color of cluster members. A number of stars display much redder colors, especially the brightest ones. The solid vertical line indicates the theoretical main sequence (see below).

The  $J - H$  versus  $H - K$  color–color plot is displayed in Figure 4. Open circles indicate objects fainter than  $J = 15$ . Open triangles indicate stars fainter than  $H = 15$  and  $J = 15$ . The numbers labeling stars in both plots refer to the same objects. The inclined lines, from top to bottom, indicate interstellar reddening directions for main sequence M–type (Frogel et al. 1978), O–type (Koornneef 1983) and T Tauri (Meyer et al. 1997) stars. Stars to the right of the solid line deviate from pure interstellar reddening, probably because of hot dust emission. The effect of this excess emission is stronger in the  $K$ –band than at shorter wavelengths. Although the open circles and triangles in the bottom right of Figure 4 indicate only lower limits, these objects are also likely affected by thermal emission. They are bright in the  $K$ –band and should be detected in  $J$  and/or  $H$  if affected only by interstellar reddening if they were cluster members with typical extinction.

##### 3.1.1. Reddening and excess emission

The cluster characteristics indicate that the stars haven’t had enough time to evolve away from the main sequence. We expect that most of the high mass stars are close to the Zero Age Main Sequence (ZAMS). We can estimate the reddening toward the cluster from a simple relation  $A_K$

$\sim 1.6 \times H - K$  based on the average color of hot stars  $H - K = -0.04$  (Koornneef 1983) and the Mathis extinction law (Mathis 1990). The stars brighter than  $K = 14$  have an average color of  $H - K = 0.98$ , corresponding to  $A_K = 1.57$  mag ( $A_V \approx 15.7$  mag). The interstellar component of the reddening can be separated from that local to the cluster stars by using the star HD 97499. This is a foreground star, since it is brighter and less reddened than stars in the cluster and is offset from the radio source line-of-sight by 2 arc-minutes. From its spectral type B1-2IV-V *Michigan Spectral Catalogue* - (Houk & Cowley 1975) and magnitude, a distance of 2.4 kpc was derived (Persi et al. 1994). Our measurements of this star result in  $H - K = 0.19$ , indicating  $A_K = 0.37$ . This gives  $A_K = 0.154 \text{ mag kpc}^{-1}$ , which is close to the expected extinction for this position along the Galactic plane. For 2.8 kpc distance of NGC3576, the interstellar component is then  $A_K = 0.43$ , leaving a local component of  $A_K = 1.14$ . We were not able to independently check the distance derived by DePree (1999) via spectroscopic parallax (see below), but we expect that the radio kinematic distance is reliable for this Galactic direction.

In order to place the ZAMS in the CMD, the corresponding bolometric magnitudes ( $M_{\text{Bol}}$ ) and effective temperatures ( $T_{\text{eff}}$ ) must be transformed into  $H - K$  colors and apparent  $K$  magnitudes. Shaller et al. (1992) models for the ZAMS with solar abundances were adopted. The bolometric corrections (BC) applied to derive absolute visual magnitudes ( $M_V$ ) are from Vacca et al. (1996) for spectral types  $O$  to  $B0$  and from Malagnini et al. (1986) for later spectral types. The intrinsic colors ( $V - K$ ,  $J - K$ , and  $H - K$ ) are from Koornneef (1983). Using the distance modulus (12.24) and the apparent visual magnitude, we transform the  $M_{\text{Bol}}$  into apparent  $K$  magnitudes. The correspondence between spectral types and  $T_{\text{eff}}$  are from Vacca et al. (1996) for  $O$  to  $B0$  and from Johnson (1966) for later spectral types. Since Koornneef’s colors are in the Johnson system, which is nearly identical to SAAO system (Carter 1990), we used the SAAO to CIT/CTIO relations to transform Koornneef’s  $H - K$  color indices to the CIT/CTIO system. These corrections are about 1% and could be neglected when compared with the photometric errors and differential reddening.

The ZAMS is represented by a vertical solid line in Figure 3, shifted to  $D = 2.8$  kpc and reddened by  $A_K = 0.43$  due to the interstellar component. When adding the average local reddening ( $A_K = 1.14$ ), the ZAMS line is displaced to the right and down, as indicated by the dashed lines. We cannot fix the position of the ZAMS, since there is a scatter in the reddening. The small group of relatively bright stars ( $K \sim 11$ ) in between these two lines, suggests that some of them, the bluer ones, could mark the position of the ZAMS. Unfortunately, we don’t yet have spectra of these objects to check whether or not this is true.

Objects to the right of the O-type stars line (Figure 4) have colors deviating from pure interstellar reddening. This is frequently seen in young star clusters and is explained by hot dust in the circumstellar environment. We can estimate a lower limit to the excess emission in the  $K$ -band by supposing that the excess at  $J$  and  $H$  is negligible, and that the intrinsic colors of the embedded stars are that of OB stars. Indeed, assuming that the observed stars are young objects (and not foreground or background stars), then the intrinsic  $H - K$  color of any object in our sample is equal to  $0.0 \pm 0.06$  mag (Koornneef 1983). Let us adopt for every object in our sample the colors of an

intermediate OB star,  $H - K = -0.04$  (Koornneef 1983), as we did above. The error in the color index is smaller than the uncertainty in the Mathis law. Errors are large for stars not detected in the  $H$ -band, for which we adopt the limiting magnitude of our detection ( $H = 15$ ). The fainter cluster members - more difficult to detect in the  $J$ -band - are the mostly affected by the errors in the de-reddening procedure. Those errors are propagated in to the excess emission whose scatter increases with magnitude, as seen in Figure 5. Objects with very large excess in the upper right corner of Figure 5, however, cannot be explained by the de-reddening procedure and could be real. They could represent the emission of accreting disks around the less massive objects of the cluster.

### 3.1.2. The KLF and the IMF

In order to separate the cluster members from projected stars in the cluster direction, we imaged a region close to NGC3576. The star counts were normalized by the relative areas projected on the sky and then binned in intervals of  $\Delta K = 0.5$  and  $\Delta(H - K) = 0.5$ . The stellar density in the field was then subtracted from that of the cluster in bins of magnitude and color intervals. This works well for foreground stars, since there were a few in the cluster field. Regarding the background, the situation is more complex, however, since NGC3576 produces so high an obscuration, almost no background objects can be seen at this limiting magnitude.

The completeness of DoPHOT detections was determined through artificial star experiments. This was accomplished by inserting fake stars in random positions of the original frame, and then checking how many times DoPHOT retrieved them. The PSF of the fake star was determined from an average of real stars found in isolation and in areas of dark sky. In total, we inserted 2400 stars in the magnitude interval  $8 \leq K \leq 20$ , which amounts to six times the number of real stars recovered in the original DoPHOT run. For every  $\Delta K = 0.5$  we inserted simultaneously 5 stars, repeating the procedure for 20 times. The insertion of all the 100 stars at once would impact the stellar crowding and change the detection conditions. The incompleteness of the sample is defined as the percentage of times the fake star fails to be recovered. We performed these experiments in the whole frame and also in each of the three sub-images that were cut out from it, displayed in Figure 1. The upper right sub-image is representative of detection limited by photon statistics, the one at the center, by high background and the lower left one, by stellar crowding. In Figure 6 we present the photometric completeness. The *dashed* line (without symbols) refers to the whole image. The limit is different for different sub-images, e.g. for an area with high nebular background (*circles*), for a crowded area (*squares*), or for an area with few stars and a dark sky (*triangles*). The performance of the photometry is better than 90% for a 15th magnitude star found in isolation, as compared to stars in the nebular zone which need to be ten times brighter to be detected with the same efficiency. Since there is no objective way to define the sub-image limits we applied a single completeness correction to the whole frame (dashed line). As seen in Figure 6 such a correction is close to the curve limited by crowding. Future work seeking to obtain deeper photometry in this cluster demands a substantial improvement of the spatial resolution and will require adaptive

optics imaging from ground based telescopes.

After correcting for non-cluster members, interstellar reddening, excess emission (a lower limit) and photometric completeness, the resulting  $K$ -band luminosity function ( $KLF$ ) is presented in Figure 7. A linear fit, excluding deviant measures by more than  $3\sigma$ , has a slope  $\alpha = 0.39 \pm 0.03$ . A similar result was obtained for W42 ( $\alpha = 0.40$ ) by Blum et al. (2000) and for the Trapezium cluster ( $\alpha = 0.43$ ) by Hillenbrand & Carpenter (2000).

We can evaluate the stellar masses by using Shaller et al. (1992) models, assuming that the stars are on the ZAMS. This is a reasonable approximation for such a young cluster. The main errors in the stellar masses are due to the effects of circumstellar emission and stellar multiplicity. Our correction to the excess emission is only a lower limit, since we assumed the excess was primarily in the  $K$  band. Hillenbrand et al. (1992) have computed disk reprocessing models which show the excess in  $J$  and  $H$  can also be large for disks which reprocess the central star radiation. In general, we can expect the excess emission to result in an overestimate of the mass of any given star and the cluster as a whole. The slope of the mass function should be less effected. It is difficult to quantify the effect of binarity on the IMF. If a given source is binary, for example, its combined mass would be larger than inferred from the luminosity of a “single” star and its combined ionizing flux would be smaller. The cluster total mass would be underestimated, the number of massive stars and the ionizing flux would be overestimated. The derived IMF slope would be flatter than the actual one.

With these limitations in mind we have transformed the KLF into an IMF. Since other authors also do not typically correct for multiplicity, our results can be inter compared, as long as this parameter doesn’t change from cluster to cluster. The  $IMF$  slope derived for NGC3576 is  $\Gamma = -1.51 \pm 0.1$  (Figure 8), which is consistent with Salpeter’s slope (Salpeter 1955). Flatter slopes have been reported only for a few clusters, most notably the Arches and Quintuplet clusters (Figer et al. 1999), both near the Galactic Center. Flatter slopes may indicate that in the inner Galaxy star forming regions, the relative number of high mass to the low mass stars is higher than elsewhere in Galaxy. It is also possible that dynamical effects may be more important in the inner Galaxy. Portegies Zwart et al. (2001) have modeled the Arches cluster data with a normal IMF, but include the effects of dynamical evolution in the presence of the Galactic center gravitational potential. They find the observed counts are consistent with an intial Salpeter-like IMF.

We derived an upper limit to the total mass of the cluster (our IMF is likely overestimated due to excess emission, see above) by integrating the  $IMF$  between  $0.08 < M/M_{\odot} < 58$  - where the distribution is nearly continuous. The lower mass limit was adopted from Hillenbrand & Hartmann (1998) taking into account the  $IMF$  turnover measured by those authors in Orion. The integrated cluster mass is  $M_{cluster} = 5.9 \times 10^3 M_{\odot}$ . As pointed out above, this is likely an upper limit.

### 3.1.3. *The Nature of NGC3576/#48*

Source #48 is anomalously bright and needs to be treated separately. Let us assume that it is affected by an interstellar reddening equal to the cluster average:  $A_K = 1.57$ , which implies a derredded magnitude  $K_0 = 6.78$ . If we take at face value the  $H - K$  color to represent only an excess at  $K$ , the reprocessing disk would contribute with  $\Delta K = -0.3$ . This excess emission is clearly an underestimation, since the stellar flux is swamped by the disk emission to the point of veiling all the photospheric lines (see below). Moreover, if the excess emission was so small, the luminosity of #48 would require a cluster of four  $100 M_\odot$  stars, unresolved down to a limit of  $0.6''$ , which doesn't seem to be the case. Alternately, we can evaluate the excess emission by using Hillenbrand et al. (1992) models for reprocessing disks. By starting with the maximum excess emission  $\Delta K = 4.05$  valid for a O7-type star (their table 4) we derive the  $M_V$ . Using Vacca et al. (1996) calibration, we obtain the corresponding stellar spectral type (and mass) that is much smaller than the O7-type we started with. The next step is reducing the excess emission (adequate for a smaller stellar luminosity), deriving a larger final mass, and iterating until convergence. This was achieved for an excess emission  $\Delta K = 3.17$ , corresponding to a spectral type BIV and mass  $M = 17 M_\odot$ . This is possibly a lower limit, since the intervening extinction toward #48 is probably larger than the cluster average. We can say that #48 is a late-O/early-B/early B YSO, very similar to what has been found by Blum et al. (2000) in W31 for the brightest  $K$ -band object in that cluster. Object #48 is buried in a large and dense disk, and its contribution to the cluster mass and ionizing photons are negligible.

We have compared the locations of the  $K$ -band sources in our images with the mid-infrared sources of (Frogel et al. 1978). Source #48 is very close to their IRS1 and #11 to their IRS3. These sources appear also in the IRAS Small Scale Structure Catalogue (X1109-610) and the IRAS Point Source Catalogue (IRAS11097-6102). In the case of IRS1, at least, recent high resolution mid-infrared images (Barbosa et al. 2002) clearly indicate that it is associated with our object #50,  $1''$  to the south of the  $K$ -band source #48.

### 3.1.4. *General Properties of the Stellar Cluster*

The properties of the cluster are summarized in Table 1. The number of Lyman continuum photons derived from the IMF is  $N_{\text{Lyc}} = 1.13 \pm 0.22 \times 10^{50} \text{ s}^{-1}$  which can be compared with that based from radio observations (De Pree et al. 1999):  $N_{\text{Lyc}} = 1.6 \pm 0.4 \times 10^{50} \text{ s}^{-1}$ . The two estimates are in agreement to within the uncertainties.

The stellar cluster is located in the NE border of a molecular cloud. The stellar density increases toward the SW, ending abruptly, with a few sources embedded in the molecular cloud (Figure 2). The spatial distribution of color indices (Figure 9) also shows a similar gradient. This is due, in part, to the increasing extinction toward the inner molecular cloud. However, the red colors are intrinsic to many of the sources, since there are excess emission objects in this zone. This

suggests that stars at the SW are younger than at NE, since recent models by Behrend & Maeder (2001) predict formation times of the same order for stars of different masses. A similar scenario for this cluster, by which star formation is progressing toward the inner zones of the molecular cloud, has been suggested by Persi et al. (1994) and De Pree et al. (1999) and our images dramatically confirm this to be the case; see Figure 2.

### 3.2. Spectra

Spectra of eight cluster members (#4, #11, #48, #69, #78, #95, #160 and #184), are shown in Figure 10 and Figure 11. Spectra of a foreground M-type and an A-type stars were added at the top of the figures for comparison. The A-type star also was divided by the average continuum slope of the other observed A-type stars.

Object labels are the same as in Figure 1; 3; and 4. Ordinates in Figure 10 and Figure 11 are normalized fluxes, as follows. We constructed templates for telluric absorption bands by observing A-type stars, close in time and airmass to the target stars. We removed the Br $\gamma$  line from those spectra by hand (linear interpolation), since this region is free from telluric features. There are no other noticeable photospheric features in A-type stars in the  $K$ -band. Then we divided the spectrum of each target by the appropriate A-type spectrum and normalized the resulting spectrum at 2.19  $\mu\text{m}$ . The signal-to-noise ratio is  $S/N \approx 40$  for #4, #11 and #95 and  $> 100$  for the other objects.

The spectra were placed on a flux scale by dividing by  $\lambda^4$  and multiplying by  $K$ -band fluxes corresponding to the  $K$ -magnitudes in Table 2. However, it is straight forward to compare the spectra ratioed to A-type continuum. It can be seen that all the cluster member candidates display rather inclined slopes, when compared to the A-type and M-type stars, those two showing almost identical slopes through the  $K$ -band. These eight stars are have large probability of being cluster members. They cannot be foreground stars, otherwise they would have flat slopes like the A or M-type stars. Could they be background stars? In principle yes, but they should be rather luminous in order to compensate for the dimming produced by the larger distance and reddening and still rivals with the brightest cluster members. We must take into account that these objects are projected toward the central part of the cluster and thus subject to high obscuration ( $A_K = 1.57$ ) due to the intra cluster gas and dust. Objects #48, #95, and #160 are undoubtedly cluster members, since, in addition, they have excess emission. Object #69 is bright in the  $H$  and  $K$  bands and judging from its  $H - K$  color, it should be relatively bright in the  $J$ -band, but it isn't detected at all in the  $J$ -band OSIRIS images, appearing above the reddening line in Figure 4. The spectrum of this object in Figure 11 looks like its neighbor #78, that is 1.5 magnitude fainter and still is detected in the  $J$ -band. This puzzling situation was clarified when we took a  $K$ -band acquisition image (Feb/2002) with Phoenix at Gemini under very good seeing ( $\sim 0.25\text{--}0.3''$ ). In that image, object #69 is shown as a small nebula, with no sign of a buried point-like source. Object #69 is a clump of dense material ionized by object #48 or some other neighboring source. The  $\text{H}_2$  2.122

$\mu\text{m}$  emission could be either shock or ionization produced.

The narrow features at 2.058 (He I) and 2.166  $\mu\text{m}$  ( $\text{Br}\gamma$ ) in Figures 10 and 11 are due to contamination from the extended nebula. The spectra were extracted in such a way that the large scale nebular component is over-subtracted. In some objects these lines are in emission, due to enhanced nebular emission close to the star. Objects #48, #160, #78 and #69 show  $\text{H}_2$  2.122  $\mu\text{m}$  in emission. This feature appears is emission also in #11 and #95, but since the He I and  $\text{Br}\gamma$  components are not over subtracted, this feature may be due to contamination of extended nebular emission. The CO bandhead at 2.2935  $\mu\text{m}$  is in absorption in #4, #160, #184 and in emission in #48. None of those objects show photospheric lines indicating that they are still enshrouded in their birth cocoons. This is corroborated by the excess emission in the  $K$ -band derived from photometry except for objects #4 and #184 (Table 2).

The CO feature is formed in dense gas. It has been observed in FU Orionis-like objects and T Tauri stars in a phase of disk accretion. It appears in absorption when the accretion rate is high and/or the disk is edge-on (Biscaya et al. 1997). Hanson et al. (1997) reported the presence of CO in several objects in M17. For objects #4 and #184 which have no strong excess emission indicated, the case for FU Orionis object or background M star is not clear.

The  $\text{H}_2$  molecular emission is produced by shocks and may indicate the existence of gas outflow. Since we subtracted the extended background close to the stars, the spectra show only the spatially unresolved component of  $\text{H}_2$ . We can thus be pretty confident that  $\text{H}_2$  emission in #48 and #69 are emitted close to the stellar sources. However, since these two sources are only  $\sim 11''$  apart, the emission could be associated with both objects or with only one of them.

It may be surprising that most of the stars with featureless spectra are close to the interstellar reddening line. However this is in accord with the Hillenbrand et al. models (1992) for early type stars, which predict relatively small color excesses ( $\Delta(H - K) < 0.5$ ) for objects with large excess emission ( $\Delta K < 4.0$ ). Such models do not predict large departure from the reddening line, like displayed by objects #160 and #50. Those sources might be surrounded by local dusty clouds, in addition to the accreting disk.

#### 4. Discussion

We have presented deep  $J$ ,  $H$  and  $K$  images of the newborn stellar cluster in NGC3576 (Figure 2) and  $K$ -band spectra for eight cluster members. The  $K$ -band excess emission displayed by objects #4, #11 (IRS3?), #48 (#48), #69, #78, #95, #160 and #184, in combination with their featureless continuum or CO emission/absorption (Figure 10), indicates that they are young, massive stars still in the process of accreting material from their birth cocoons. The lack of photospheric features and presence of disk signatures indicates that among the newborn massive star clusters in the Milky Way, NGC3576 is one of youngest.

Our data also confirm the scenario of star formation progressing from the NE toward the inner parts of the molecular cloud (SW), but the very young age of the cluster may contradict the claim of enhanced He abundance in the NE part of the GH II region by De Pree et al. (1999). There are no evolved stars in the cluster which could produce the enhancement and the time to diffuse nuclear processed material from neighboring regions into the nebular environment would be much larger than the cluster age. The fact that the nebular excitation increases toward the NE, producing stronger He lines, may have influenced the abundance calculations.

Since our data do not enable us to derive spectroscopic parallaxes (no photospheric lines were detected in the luminous stars), we have adopted the radio distance obtained by De Pree et al. (1999) revised to 2.8 kpc by using the most recent Galactic center distance ( $R_0 = 8$  kpc, (Reid 1993)). The cluster parameters are not well constrained because of distance uncertainty and the difficulty in correcting the  $K$ -band magnitude for the circumstellar dust emission and extinction. However, the overall picture summarized in Table 1 of a massive and dense cluster remains valid. Moreover, the ionizing flux derived from the IMF agrees, within the errors, with that derived from radio observations.

The fact that several of the brightest cluster members do not show naked photospheres raises the question: where are the ionizing sources of NGC3576? It is plausible that some of the faint sources are in reality luminous objects under heavy extinction, and were not properly dereddened because they escaped detection in the  $J$  and  $H$ -band. This may also explain why the number of Lyman continuum photons derived from the IMF is smaller than that measured at radio wavelengths. To tackle this question, we plan to obtain spectra from stars of  $K \approx 13$ , which demands a 8-m class telescope.

In order to understand better the circumstellar environment of the YSOs we examined here, we have performed high resolution mid-infrared imaging with the Gemini South telescope which will be analyzed in a future paper. Our goal is to derive the characteristics of the circumstellar dust, in particular evaluating its contribution to the near infrared excess emission, extinction, and the possible presence of accreting disks.

EF and AD thank FAPESP and PRONEX for support. PSC appreciates continuing support from the National Science Foundation.

## REFERENCES

- Barbosa, C., D., R. et al., 2002, in preparation.
- Behrend, R. & Maeder, A., 2001, A&A, 373, 555
- Biscaya, A. M., Rieke, G. H., Narayanan, G., Luhman, K. L., Young, E. T. 1997,
- Blum, R. D., Daminieli, A., Conti, P. S. 1999, AJ, 117, 1392

- Blum, R. D., Conti, P. S., Daminieli, A. 2000, *AJ*, 119, 1860
- Blum, R. D., Daminieli, A., Conti, P. S. 2001, *AJ*, 121, 3149
- Carter, B. S., 1990, *MNRAS*, 242, 01
- Caswell, J. L., Batchelor, R. A., Forster, J. R., Wellington, K. J. 1989, *Australian J. Phys.*, 42, 331
- Caswell, J. L., Vaile, R. A., Ellingsen, S. P., Whiteoak, J. B., Norris, R. P., 1995, *MNRAS*, 272, 96
- Blum, R. D., & Conti, P. S. 2002, *ApJ*, 564, 827
- DePoy, D. L., Atwood, B., Byard, P., Frogel, J. A., & O'Brien, T., 1993, *Proc. SPIE*, 1946, 667
- De Pree, C. G., Nysewander, M. C., Goss, W. M. 1999, *AJ*, 117, 2902
- Elias, J. H., Frogel, J. A., Matthews, K., & Neugebauer, G., 1982, *AJ*, 87, 1029
- Figer, D. F., Kim, S. S., Morris, M., Serabyn, E., Rich, R. M., McLean, I. S., 1999a, *AJ*, 525, 750
- Frogel, J. A., Persson, S. E., Matthews, K., Aaronson, M. 1978, *ApJ*, 220, 75
- Goss, W. M. & Radhakrishnan, V. 1969, *Astrophys. Lett.*, 4, 199
- Goss, W. M. & Shaver, P. A., 1970, *Australian J. Phys. Astroph. Suppl.*, 14, 1
- Johnson, H. L. 1966, *ARA&A*, 04, 193
- Hanson, M. M., Conti, P. S., Rieke, M. J. 1996, *ApJS*, 107, 281
- Hanson, M. M., Howarth, I. D. , Conti, P. S. 1997, *ApJ*, 489, 698
- Hillenbrand, L. A., Strom, S. E., Vrba, F. J., & Keene, J. 1992, *ApJ*, 397, 613
- Hillenbrand, L. A., Hartmann, L. W. 1998, *ApJ*, 492, 540
- Hillenbrand, L. A., Carpenter, J. M., 2000, *ApJ*, 540, 236
- Houk, N. & Cowley, A. P. 1975 *Michigan Spectral Catalogue, Vol. 1 (Univ. Michigan: Ann Arbor)*
- Koornneef, J. 1983, *A&A*, 128, 84
- Lada, C. J., DePoy, D. L., Merrill, K. M., Gatley, I., 1991, *ApJ*, 374, 533
- Lada, C. J., Adams, F. C., 1992, *ApJ*, 393, 278
- Malagnini, M. L., Morossi, C., Rossi, L., Kurucz, R. L. 1986, *A&A*, 162, 140
- Mathis, J. S. 1990, *ARA&A*, 28, 37
- McGee, R. X., Gardner, F. F., 1968, *Australian J. Phys.*, 21, 149

- McGee, R. X., Newton, L. M., 1981, MNRAS, 196, 889
- Meyer, M. R., Calvet, N., Hillenbrand, L. A. 1997 AJ, 114, 288
- Moorwood, A. F. M., & Salinari, P. 1981, A&A, 102, 197
- Okumura, S., Mori, A., Nishihara, E., Watanabe, E. & Yamashita, T. 2000, ApJ, 543, 799
- Olivia, E. & Origlia, L. 1992, A&A, 254, 466
- Persi, P., Roth, M., Tapia, M., Ferrari-Toniolo, M. Marenzi, A. R., 1994 A&A, 282, 474
- Persson, S. E., Murphy, D. C., Krzeminski, W., & Roth, M., 1998, AJ, 116, 2475
- Portegies Zwart, S. F., Makino, J., McMillan, S. L. W., & Hut, P. 2001, astro-ph/0102259
- Reid, M. J. 1993, ARA&A, 31, 345
- Salpeter, E. E. 1955, ApJ, 121, 161
- Schaller, G., Schaerer, D., Meynet, G., Maeder, A. 1992, A&AS, 96, 269
- Schecter, P. L., Mateo, M. L., & Saha, A., 1993, PASP, 105, 1342
- Vacca, W. D., Garmany, C. D., Shull, J. M. 1996, ApJ, 460, 914
- White, G. J. & Phillips, J. P., 1983 MNRAS, 202, 255
- Wilson, T. L., Mezger, P. G., Gardner, F. F., Milne, D. K., 1970 A&A, 6, 364

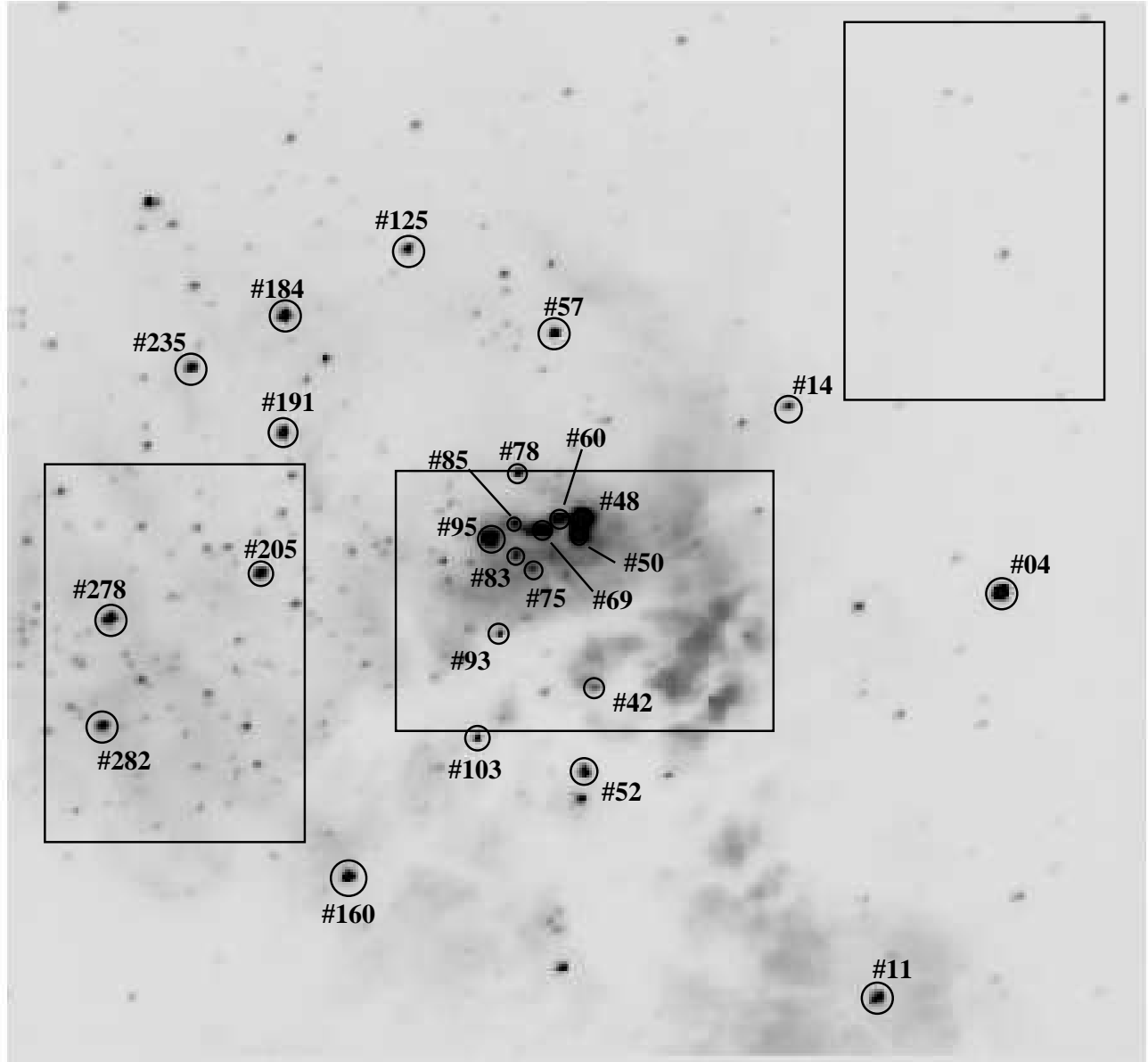


Fig. 1.— Finding chart using a  $K$ -band image of NGC3576. The *square symbols* are for stars whose spectra are displayed in Figures 10 and 11. North is up and East to the left. The coordinates of the center of the image are RA (2000) = 11h11m53.6s and Dec. =  $-61^{\circ}18'20.8''$  and the size of the image is  $1.77' \times 1.65'$ . The rectangular boxes indicate image sub-sections used to perform artificial star experiments (see text).



Fig. 2.— False color image of NGC3576:  $J$  is blue,  $H$  is green and  $K$  is red. North is up and East to the left.

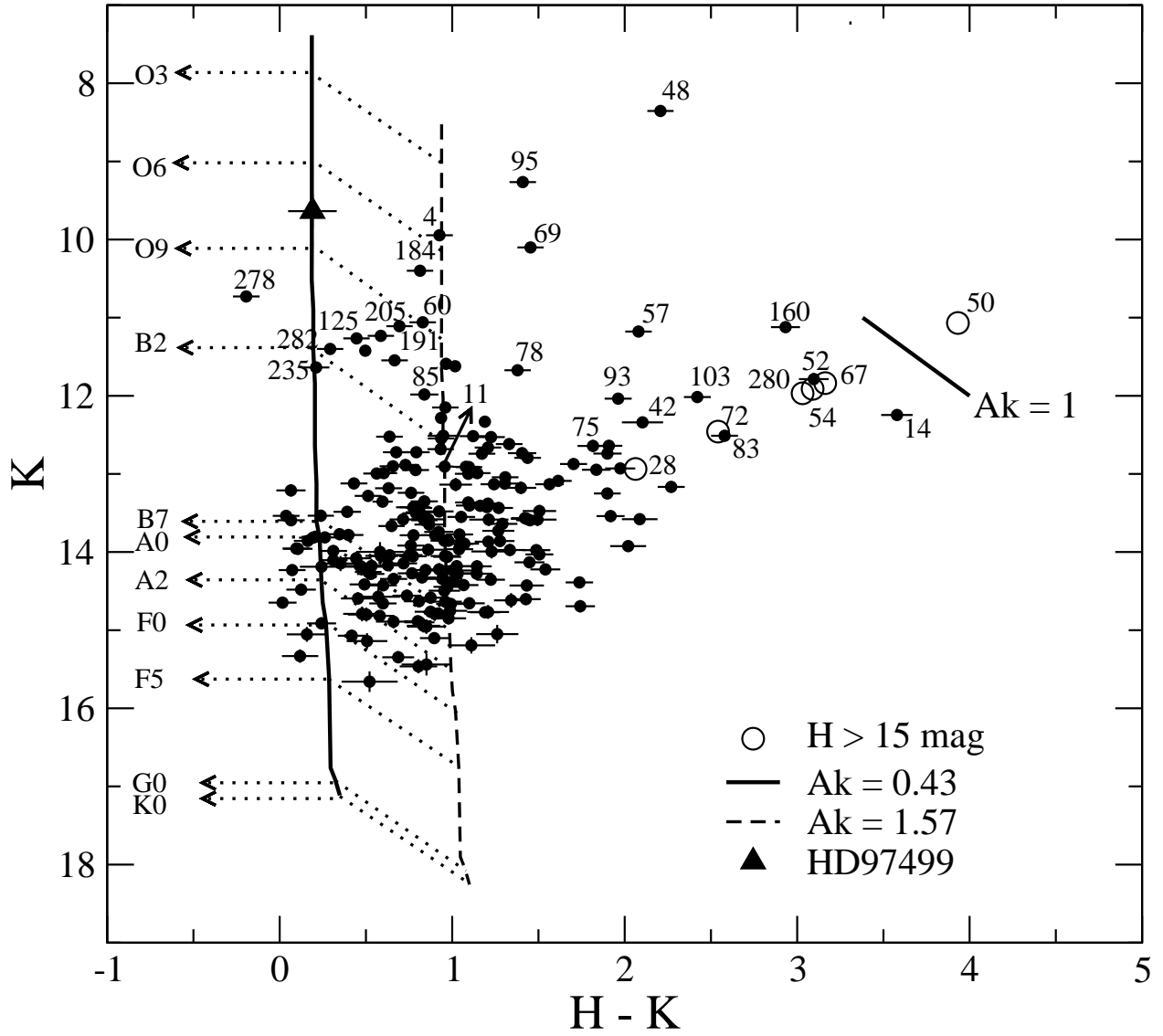


Fig. 3.—  $K$  vs  $H - K$  color-magnitude diagram (CMD) showing the ZAMS at  $D = 2.8$  kpc and  $A_K = 0.43$ . The *open circles* indicate no detection in the  $H$  band to a limiting magnitude of  $H = 15$ . Object labels are the same as in Figure 1.

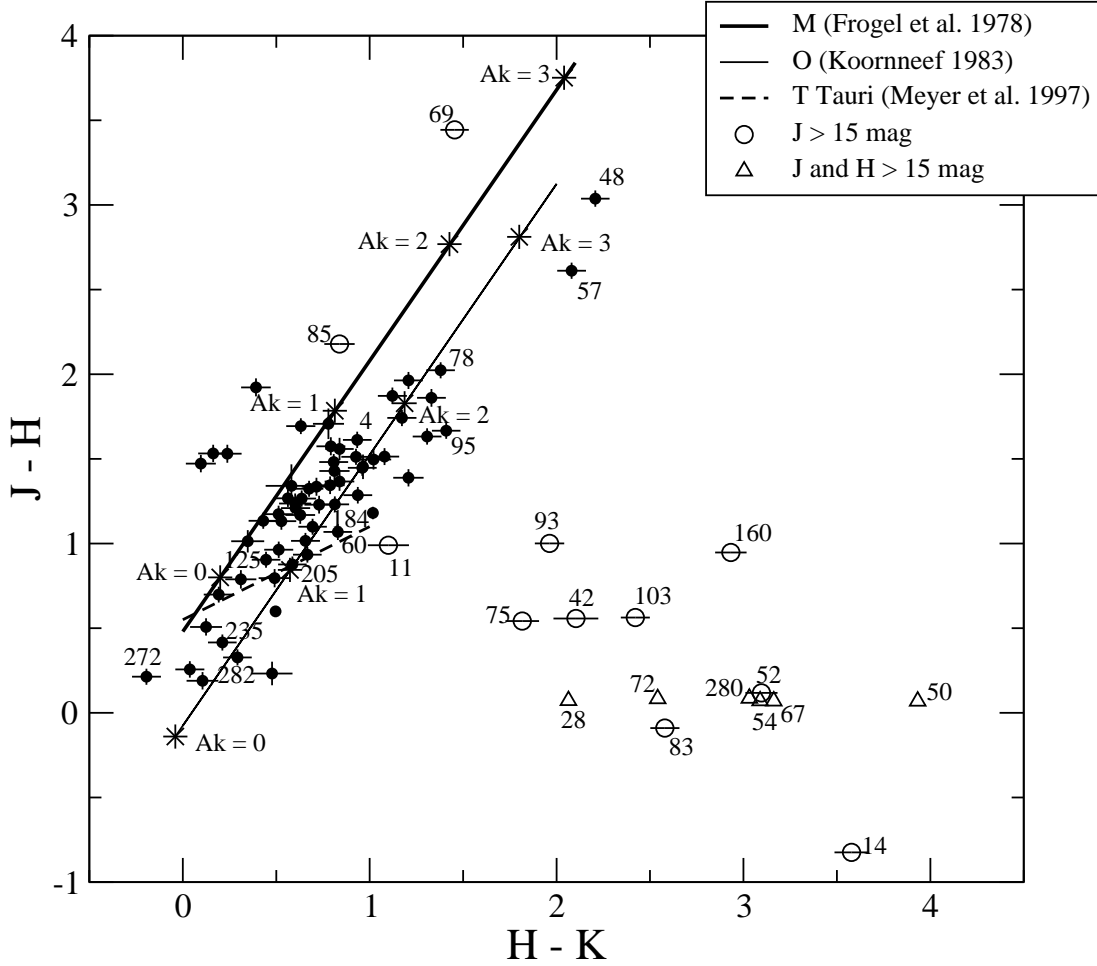


Fig. 4.—  $J - H$  vs  $H - K$  color-color plot showing the reddening line of M-type stars (*heavy solid line*), O-type stars (*solid line*) and T Tauri stars (*dashed line*). *Open triangles* indicate stars with  $J$  and  $H > 15$ ; *open circles*, stars with  $J > 15$ . The *stars* refer to  $A_K$  reddening. Object labels are the same as in Figure 1.

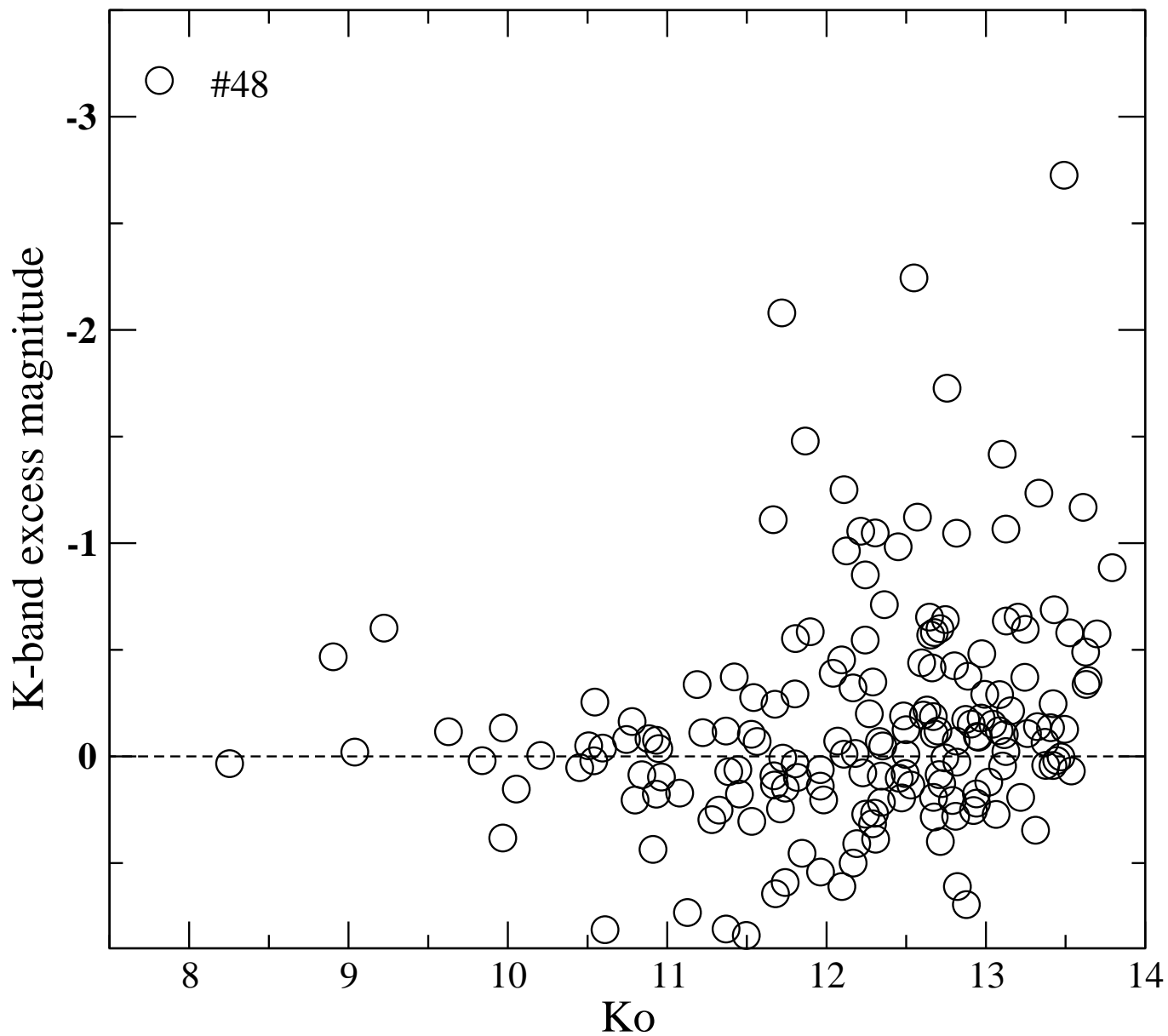


Fig. 5.— Excess emission as a function of dereddened  $K$ -band magnitude ( $K_0$ ). Very negative values represent circumstellar emission.

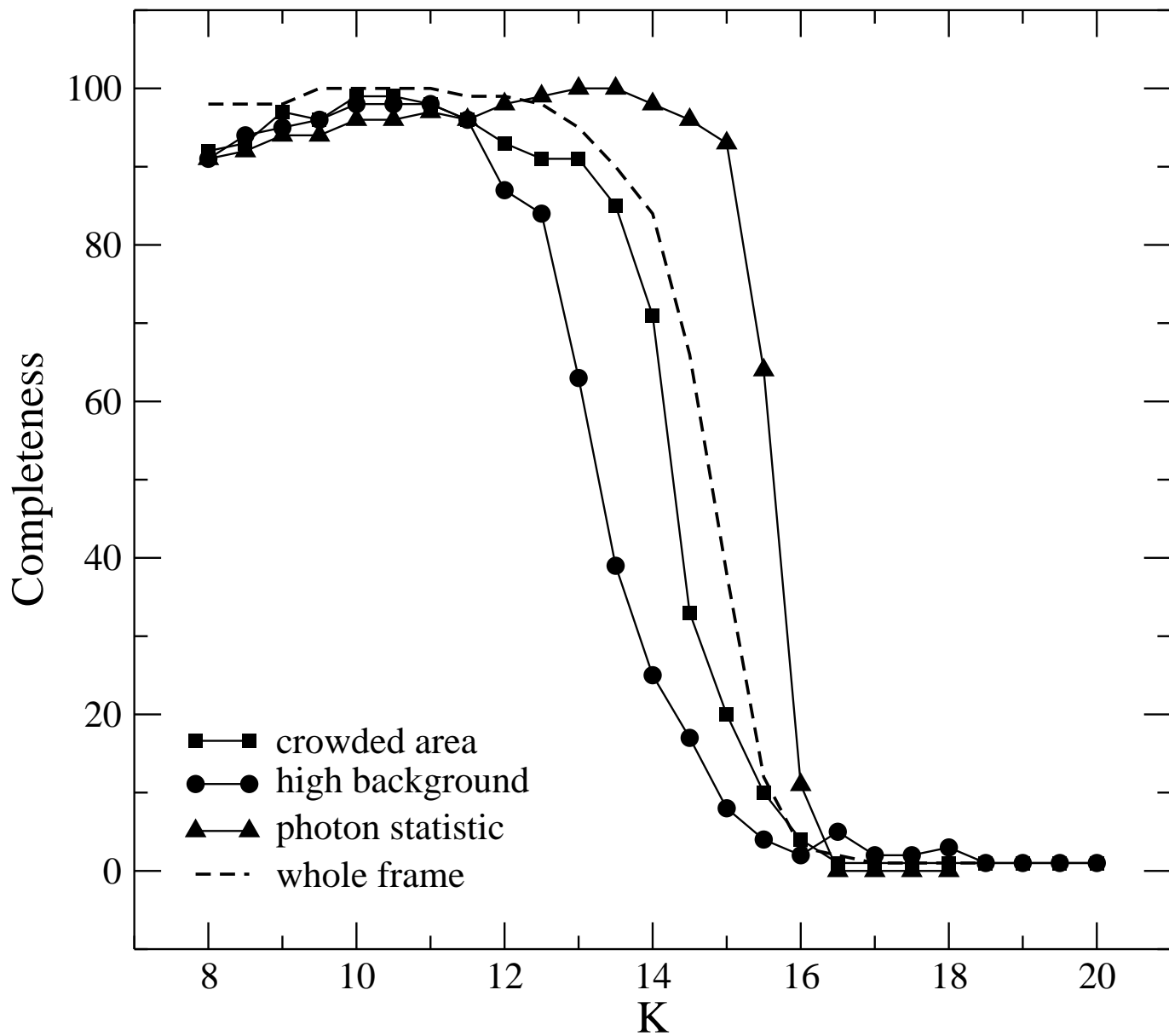


Fig. 6.— Completeness (in percent detection) as derived from artificial star experiment. The *dashed* line is for the whole frame and the symbols are for representative sub-regions of the frame; see text.

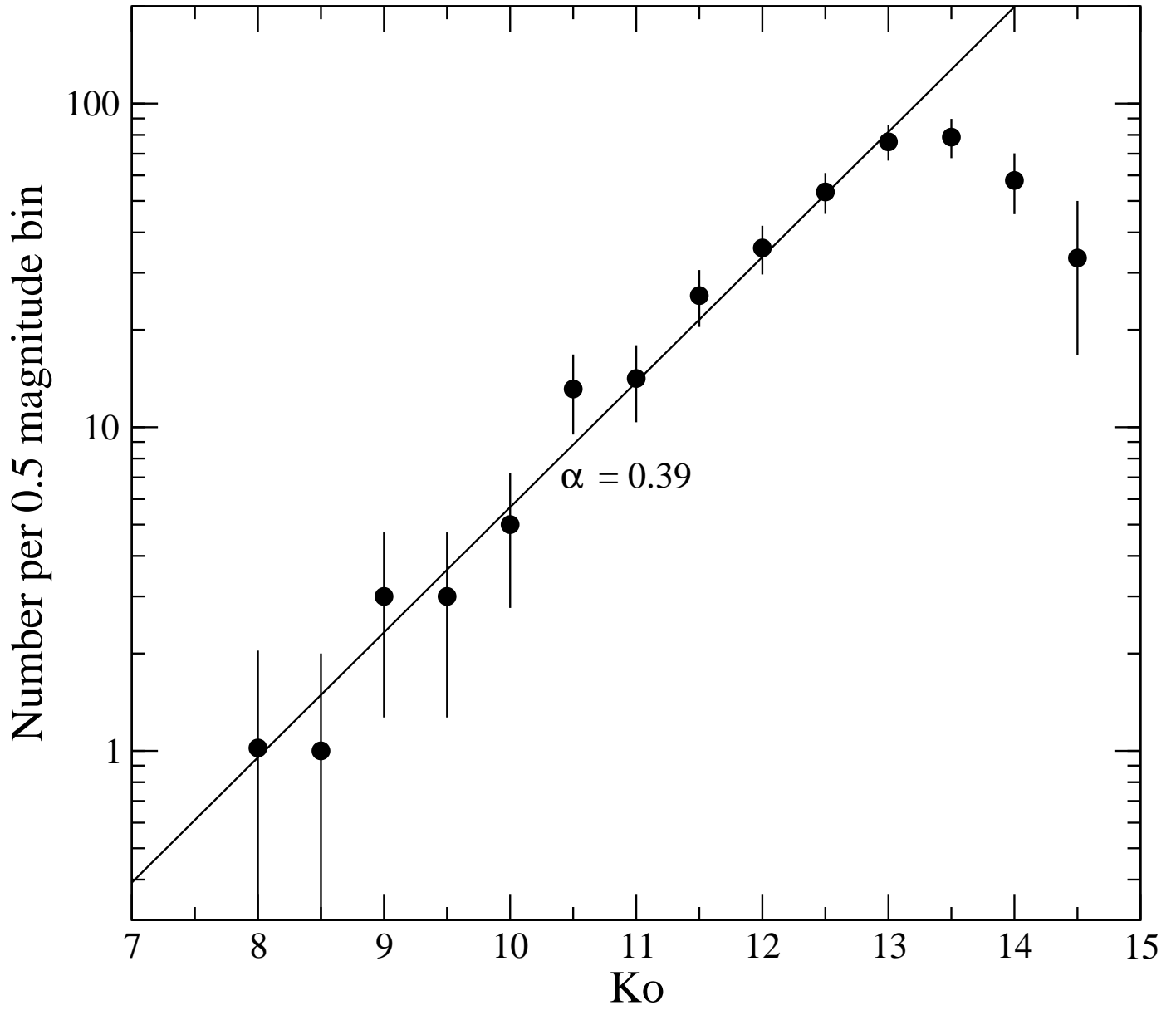


Fig. 7.— The  $K$ -band luminosity function corrected for non-members and sample incompleteness.  $K_o$  is dereddened and corrected for excess emission; see text.

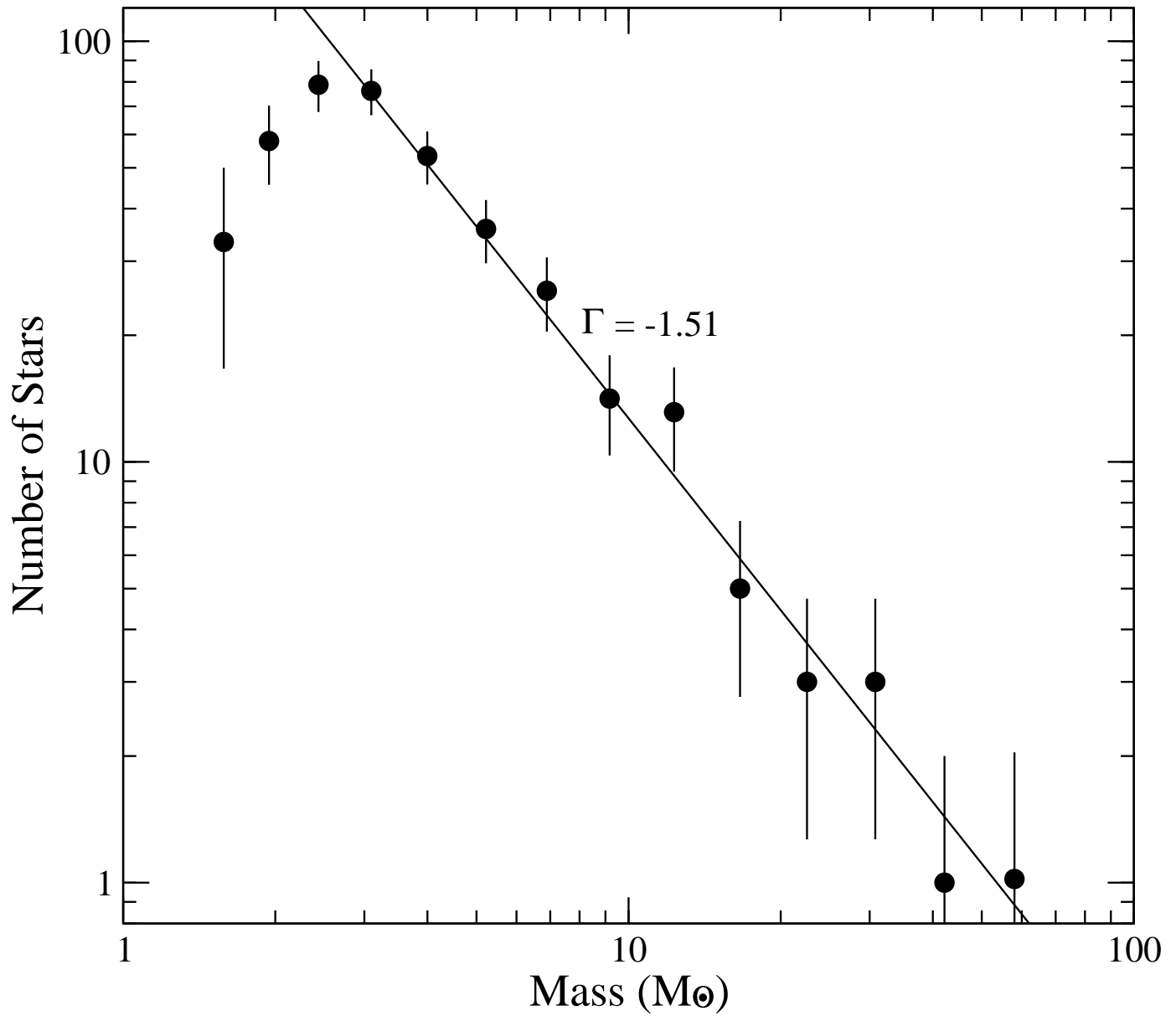


Fig. 8.— The IMF of the cluster members using the models of Shaller et al. (1992) and the KLF from Figure 7.

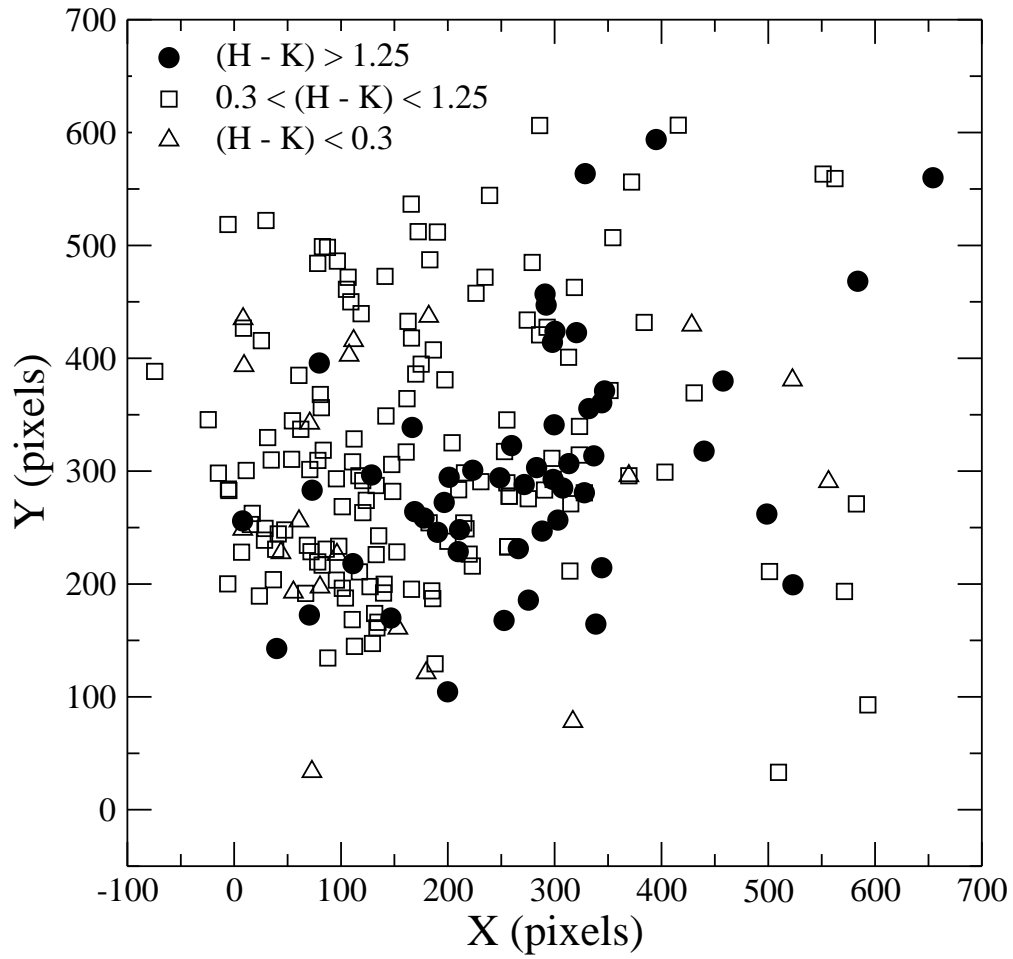


Fig. 9.— Spatial distribution of the  $H - K$  color index. North is up and East to the left. An increase in the color excess is seen toward SW (bottom right).

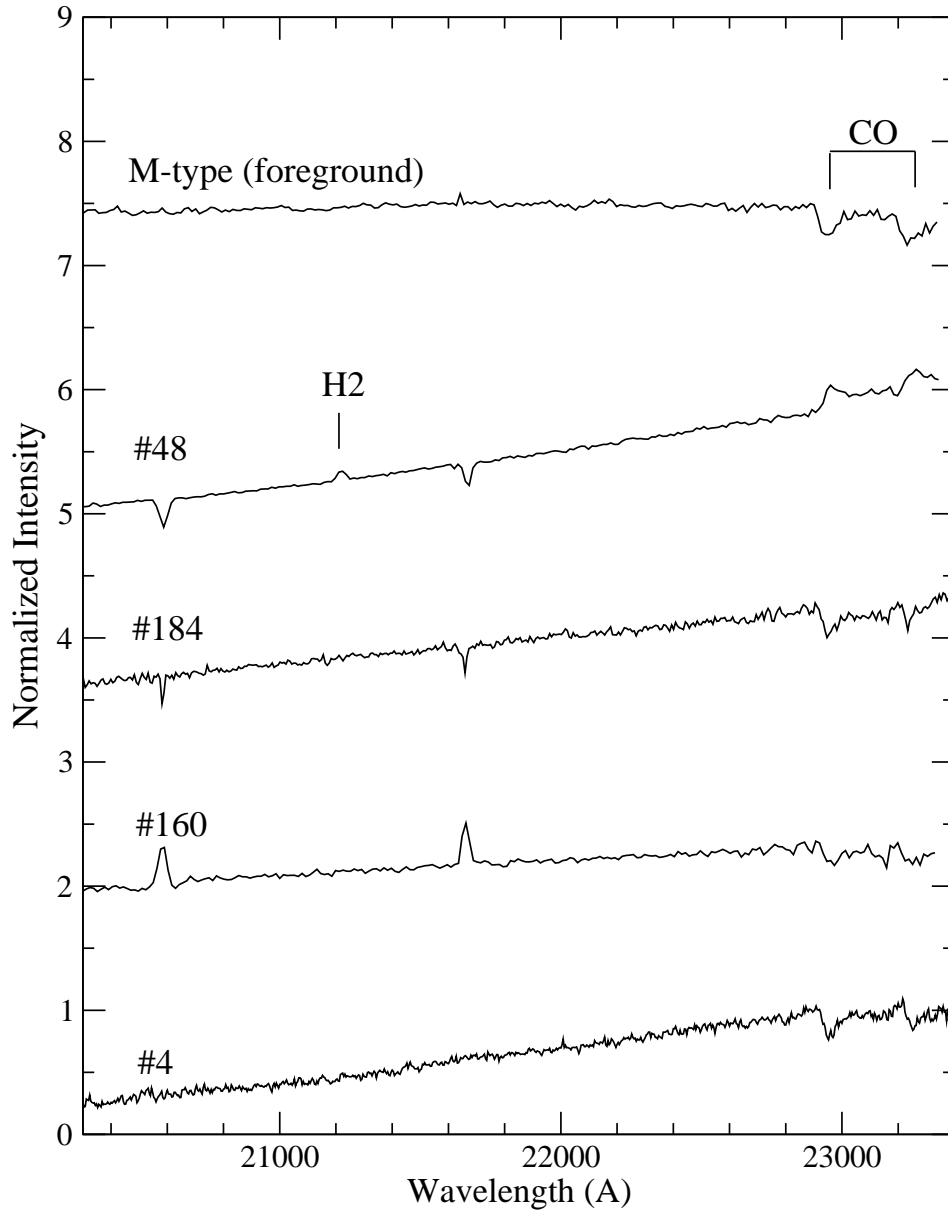


Fig. 10.— Spectra of four cluster members displaying featureless continuum superimposed on CO emission (#48) or absorption (#184, #180 and #4). Star #48 also shows H<sub>2</sub> in emission even after oversubtracting He I and Br $\gamma$  nebular component. The spectrum at the top is a foreground M-type star. Fluxes were divided by an A-type star and normalized to unity at 2.19  $\mu$ m. Stars #48 and #160 were observed with the IRS and stars #4, #48 and #184 with OSIRIS.

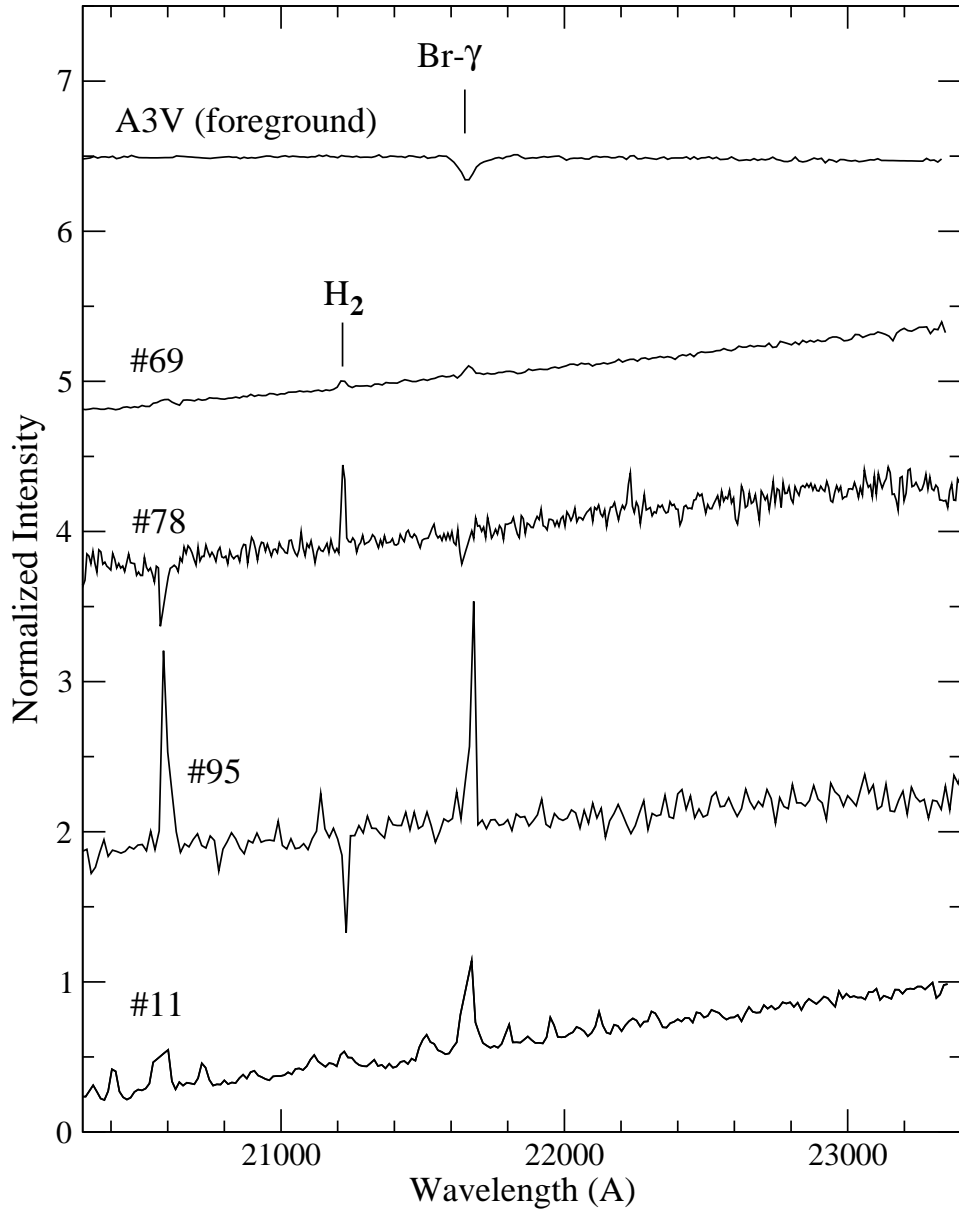


Fig. 11.— Spectra of four cluster members displaying featureless continua. Objects #11, #69, #78 show  $H_2$  in emission. The absorption feature in #95 is due to over subtraction of the nebular component. Stars #11 and #69 were observed with the IRS and stars #78 and #95 with OSIRIS. Fluxes were divided by the average continuum of several A-type stars and normalized to unity at  $2.19 \mu\text{m}$ . The spectrum at the top is a foreground A3V-type star (also divided by the average A-type star continuum).

Table 1. Cluster Properties

Cluster distance	$2.8 \pm 0.3$ kpc
Cluster diameter	1.5 pc
Cluster mass	$<5.9 \times 10^3 M_{\odot}$
Stellar density	$<2.5 \times 10^3 M_{\odot} \text{ pc}^{-3}$
IMF slope	$\Gamma = -1.51$
NLyc phot. (IMF)	$1.13 \pm 0.22 \times 10^{50} \text{ s}^{-1}$
NLyc phot. (radio)	$1.6 \pm 0.4 \times 10^{50} \text{ s}^{-1}$

Table 2. YSO properties

ID	$J - H^a$	$H - K^a$	$K^a$	K-exc <sup>b</sup>	Note
#4	1.51	0.93	9.95	+0.03	CO abs
#11	>0.99	1.10	12.91	-0.24	
#48	3.04	2.21	8.35	-3.17	H <sub>2</sub> & CO em
#69	>3.44	1.45	10.10	-0.60	H <sub>2</sub> em
#78	2.02	1.38	11.67	-0.12	H <sub>2</sub> em
#95	1.67	1.41	9.26	-0.36	
#160	>0.95	2.93	11.12	-2.08	CO abs
#184	1.23	0.81	10.40	-0.02	CO abs

<sup>a</sup>Non-derredded magnitudes; errors ( $J - H \pm 0.05$ ,  $H - K \pm 0.08$ ,  $K \pm 0.07$ )

<sup>b</sup>Excess magnitude in the  $K$ -band after derreddening